

Phase-Field Study of Polycrystalline Growth and Texture Selection During Melt Pool Solidification

Rouhollah Tavakoli and Damien Tournet

IMDEA Materials, Getafe, Madrid, SPAIN

E-mail: rouhollah.tavakoli@imdea.org, damien.tournet@imdea.org

Abstract. Grain growth competition during solidification determines microstructural features, such as dendritic arm spacings, segregation pattern, and grain texture, which have a key impact on the final mechanical properties. During metal additive manufacturing (AM), these features are highly sensitive to manufacturing conditions, such as laser power and scanning speed. The melt pool (MP) geometry is also expected to have a strong influence on microstructure selection. Here, taking advantage of a computationally efficient multi-GPU implementation of a quantitative phase-field model, we use two-dimensional cross-section simulations of a shrinking MP during metal AM, at the scale of the full MP, in order to explore the resulting mechanisms of grain growth competition and texture selection. We explore MPs of different aspect ratios, different initial (substrate) grain densities, and repeat each simulation several times with different random grain distributions and orientations along the fusion line in order to obtain a statistically relevant picture of grain texture selection mechanisms. Our results show a transition from a weak to a strong $\langle 10 \rangle$ texture when the aspect ratio of the melt pool deviates from unity. This is attributed to the shape and directions of thermal gradients during solidification, and seems more pronounced in the case of wide melt pools than in the case of a deeper one. The texture transition was not found to notably depend upon the initial grain density along the fusion line from which the melt pool solidifies epitaxially.

1. Introduction

The competition of columnar grains during directional solidification of metallic alloys occurs in many industrial processes like welding and additive manufacturing. It may promote the formation of a specific texture, and consequently the anisotropy in the mechanical properties of final products. In addition to melt convection and crystal nucleation ahead of the solid-liquid interface, the interactions between columnar grains mainly depend on the applied thermal field and physical properties of the material. According to the classical theory by Walton and Chalmers [1], dendritic grains with their preferred dendritic growth direction better aligned with the temperature gradient are favored during the growth competition. While this theory was applied to a wide range of applications with a reasonable outcome, experimental works [2, 3, 4] revealed that growth competition mechanisms are more complicated in practice. Recent phase-field (PF) studies on bi-crystal growth competition under a one-dimensional linear temperature field [5, 6, 7], have provided major insight in the fundamental understanding of grain growth competition mechanisms. However, simulations of dendritic grain growth competition in non one-dimensional temperature fields, with the level of accuracy afforded by PF, remain scarce [8, 9]. Here, we use parallel quantitative PF modeling to study columnar grain growth

competition under a more general thermal condition. For this purpose, we consider the epitaxial polycrystalline solidification in the transverse cross-section of a melt pool corresponding to the selective laser melting (SLM) of a Nickel-based alloy. In particular, we explore the effect of the melt pool aspect ratio and the initial (substrate) grain size upon the selection of grain orientations and texture in the solidified melt pool.

2. Methods

While we explore a broader range of conditions, the models and simulations used here are similar in nature to those already presented and discussed in previous publications [8, 9]. Therefore, here we only remind some of the main features of the modeling framework. For more details, the reader is invited to refer to these prior works.

Essentially, we first calculate the alloy thermophysical data by computational thermodynamics using the CALculation of PHase Diagram (CalPhaD) approach. Then, we perform the macro-scale thermal analysis of SLM process to determine the temperature field in and around the melt pool. Finally, we use the resulting thermal profile and history to simulate the solidification microstructure with phase-field simulations at the micro-scale. A one-way approach is used to link macro- and micro-scale simulations.

2.1. Computational alloy thermodynamics

The temperature-dependent density, $\rho(T)$, enthalpy density, $h(T)$, and effective heat capacity, $dh(T)/dT$ are computed by the CalPhaD approach (software ThermoCalc, database TCNI8). The phase diagram information is also computed by CalPhaD using a dilute pseudo-binary approximation of Inconel 718 (IN718) multi-component alloy. There are many different ways to perform a pseudo-binary approximation of a multi-component alloy [10]. Following [11], we consider Ni-5wt%Nb as the pseudo-binary surrogate for IN718. To make this approximation consistent with the transformation temperatures of the full alloy, first we compute the equilibrium liquidus temperature of IN718, T_L . Then, the partition coefficient of Nb, $k = c_s/c_l$, in IN718 is calculated at T_L , with c_s and c_l the Nb concentration in the solid and liquid phases, respectively. Finally, we calculate the slope of the liquidus line of the pseudo-binary phase diagram, m , at T_L as $m = -dT_L/dc$ where c denotes the concentration of Nb in IN718. The rest of the phase diagram data is readily obtained using the linear phase diagram assumption [8].

2.2. Macroscopic thermal simulation

Ignoring the effect of melt convection, the temperature history in the melt pool is computed by the numerical solution of the following heat transfer equation [12] in the macro-scale spatial domain, Ω_M ,

$$\rho(T) \frac{dh(T)}{dT} \frac{\partial T}{\partial t} = \nabla \cdot (K(T) \nabla T) \quad (1)$$

The temperature-dependent thermal conductivity, $K(T)$, is tabulated from [13]. The spatial domain, Ω_M , is a parallelepiped of dimensions $5 \times 2 \times 2$ mm³ along x, y, and z directions, respectively. Prior numerical convergence and size analysis [8] revealed that the resulting thermal field for a single track in its quasi-steady state was essentially independent of the domain size beyond these dimensions. The following boundary condition is applied on the top surface of Ω_M ,

$$-K(T) \nabla T \cdot \mathbf{n} = h_a(T - T_a) + \epsilon_R \sigma_R (T^4 - T_a^4) + \frac{2\eta P}{\pi r_b^2} \exp\left(\frac{2d(x, z, t)^2}{r_b^2}\right) \quad (2)$$

where \mathbf{n} denotes the unit outward vector on boundaries of Ω_M , h_a the convective heat transfer coefficient, T_a the ambient temperature, ϵ_R , the thermal radiation coefficient, σ_R the Stefan-Boltzmann constant, P the total laser power, η the power absorption coefficient, r_b the laser

beam radius and d denotes the distance to the beam center. Assuming the initial location of the laser is denoted by $(x_0, z_0)^T$ on the top surface, then for every point $(x, z)^T$ on this surface, d is computed by $d(x, z, t) = \sqrt{(x - x_0 - Vt)^2 + (z - z_0)^2}$, where V denotes the scanning velocity. Importantly, neglecting fluid flow limits the applicability of our macroscopic analysis to low laser input energy density, i.e. conduction mode, and it may not be as adequate for keyhole regime. Another effect of fluid flow might be local temperature heterogeneities in the mushy zone, which are not represented with the elliptical temperature field approximation described further below.

Along the bottom surface, the powder bed is sitting on a substrate with thermal properties of stainless steel [8] and its inferior surface at $T = T_a$. The thermal properties of the powder bed are extrapolated from that of the dense material, considering average particle diameter, powder-bed compactness, inter-particle view factor, and properties of the surrounding gas (Argon) [8]. The temperature-dependent properties of the material switch from powder-bed to dense (fluid or solid) state when the local temperature first exceeds the alloy liquidus temperature. A zero heat flux condition is applied on the other boundaries. We solve Eq. (1) by the finite element method with a first-order Euler implicit scheme in time and trilinear hexahedral elements in space, using a uniform spatial mesh of element size $20 \mu\text{m}$. Starting from the initial temperature T_a , the simulation runs until the temperature field reaches to the quasi steady-state conditions. Following Ref. [8], for our reference case, we used $P = 100 \text{ W}$ and $V = 0.1 \text{ m/s}$, with $r_b = 35 \mu\text{m}$, $h_a = 15 \text{ W/m}^2/\text{K}$, $T_a = 273 \text{ K}$, $\epsilon_R = 0.3$, and $\eta = 0.55$.

Considering the location of the solidus isotherm, we denote x_c and x_e the x -coordinate of the deepest point and of the the tail of melt pool with respect to the frame moving with the scanning velocity. We then perform the two-dimensional phase-field simulation for (y, z) cross-sections of melt pool in the time interval $(0, t_f]$ where $t_f = |x_c - x_e|/V$. For the sake of computational performance, we fit an analytical function to the temperature field in the (y, z) -plane. For this purpose, the temperature is interpolated radially between the solidus temperature and the temperature at the center of melt pool $T(x_c, y_0, z_0)$. The solidus isotherm is approximated as a half-ellipsis, and the central temperature is approximated using analytical functions — initially extrapolating radially to match reasonably the location of the liquidus isotherm, then transitioning toward a constant cooling rate as the melt pool center cools down below the liquidus temperature [9]. For the reference case, directly fitted to the finite element results, the initial (maximal) half-depth and half-width of the solidus isotherm are $d_S = 96 \mu\text{m}$ and $w_S = 128 \mu\text{m}$, respectively. Figure 1 shows the considered evolution of the elliptically approximated solidus and liquidus isotherms in the (y, z) cross-section as the melt pool shrinks, considering these reference melt pool dimensions. In order to study the effect of melt pool geometry on the columnar grain growth competition, we simply multiply (w_S, d_S) by factors $(0.5, 2.0)$, $(1.0, 1.0)$, and $(2.0, 0.5)$ for the deep, reference, and wide melt pool scenarios, respectively.

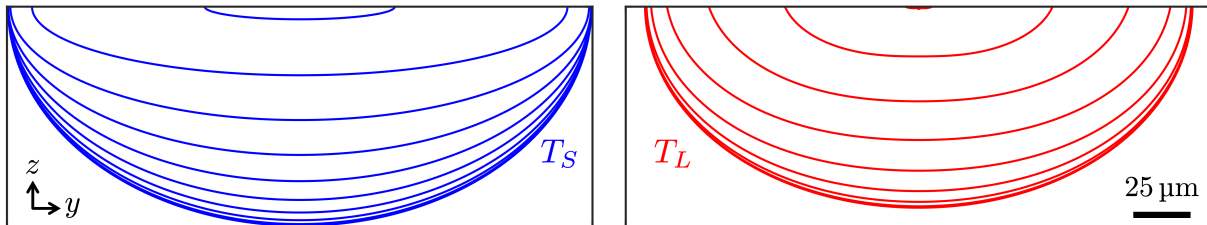


Figure 1. Time evolution of solidus (left) and liquidus (right) isotherms in the (y, z) -plane showing the shrinking of the melt pool. (Time increment between consecutive isotherms: $250 \mu\text{s}$.)

2.3. Microscopic grain growth simulation

2.3.1. *Phase-field model:* We use a classical quantitative phase-field model for dilute binary alloys solidification introduced in Ref. [14], with a non-linear preconditioning of the phase-field [15] to reduce numerical mesh dependency. The resulting form of the equations can be written

$$\begin{aligned} \left(1 - \frac{T - T_0}{mc_l^0}\right) a_s(\theta)^2 \frac{\partial \psi}{\partial t} &= \nabla [a_s(\theta)^2] \cdot \nabla \psi + a_s(\theta)^2 \left[\nabla^2 \psi - \phi \sqrt{2} |\nabla \psi|^2 \right] - \\ &\quad - \frac{\partial}{\partial z} \left[a_s(\theta) a'_s(\theta) \frac{\partial \psi}{\partial y} \right] + \frac{\partial}{\partial y} \left[a_s(\theta) a'_s(\theta) \frac{\partial \psi}{\partial z} \right] \\ &\quad + \sqrt{2} \phi - \sqrt{2} \lambda (1 - \phi^2) \left(U + \frac{T(z, y, t) - T_0}{mc_l^0(1 - k)} \right) \end{aligned} \quad (3)$$

$$\begin{aligned} \left(\frac{1+k}{2} - \frac{1-k}{2} \phi \right) \frac{\partial U}{\partial t} &= \nabla \cdot \left(\tilde{D} \frac{1-\phi}{2} \nabla U + [1 + (1-k)U] \frac{(1-\phi^2)}{4} \frac{\partial \psi}{\partial t} \frac{\nabla \psi}{|\nabla \psi|} \right) \\ &\quad + [1 + (1-k)U] \frac{(1-\phi^2)}{2\sqrt{2}} \frac{\partial \psi}{\partial t} \end{aligned} \quad (4)$$

where $T(z, y, t)$ denotes the temperature field that comes from the macro-scale simulation results, ϕ the phase-field variable, ψ the preconditioned phase-field variable, $\phi(z, y, t) = \tanh(\psi(z, y, t)/\sqrt{2})$, $\theta = \arctan(\partial_y \psi / \partial_z \psi)$ the angle between the interface normal and the horizontal axis, U the dimensionless supersaturation, $U = \frac{1}{1-k} \left(\frac{2c/c_l^0}{1-\phi+k(1+\phi)} - 1 \right)$, and c the solute concentration field, $c_l^0 = c_\infty/k$ the solute concentration of a flat interface at the reference (solidus) temperature T_0 for an alloy of nominal solute concentration c_∞ . In Eqs (3)-(4), space is scaled in units of the diffuse interface width, W , and time is scaled in units of the relaxation time, τ_0 , at T_0 [14]. The capillarity length, d_0 , is computed at T_0 [14], $d_0 = \Gamma / (|m|c_\infty(1/k - 1))$, where Γ denotes the Gibbs-Thomson coefficient of the solid-liquid interface. The non-dimensional value for the liquid diffusion coefficient, \tilde{D} , and the coupling factor, λ , are computed according to the following identities: $\tilde{D} = D\tau_0/W^2 = a_1 a_2 W/d_0$, $\lambda = a_1 W/d_0$, where D denotes the liquid diffusion coefficient, $a_1 = 5\sqrt{2}/8$ and $a_2 = 47/75$. We use a standard form of the fourfold anisotropy of the surface tension $\gamma(\bar{\theta}) = \bar{\gamma} a_s(\bar{\theta})$, with $a_s(\bar{\theta}) = 1 + \epsilon_4 \cos(4\bar{\theta})$, where $\bar{\gamma}$ is the average surface tension in a $\langle 10 \rangle$ plane, ϵ_4 is the strength of the surface tension anisotropy, and $\bar{\theta}$ is the angle between the normal to the interface and a fixed crystalline axis. For a crystal misorientation α_0 with respect to the coordinate axes, the anisotropy as function of θ between the interface normal and the x -axis follows $a_s(\theta) = 1 + \epsilon_4 \cos(4(\theta - \alpha_0))$. As the considered laser speed is relatively low ($V = 0.1$ m/s), the solid-liquid interface is assumed to remain under local equilibrium conditions. Therefore, the model does not consider kinetic undercooling or solute trapping, such that τ_0 is computed as $\tau_0 = a_2 \lambda W^2/D$, and W is the only model parameter that should be appropriately chosen for the purpose of quantitative prediction. As in Refs [8, 9], the material properties for the Ni-Nb (IN718 surrogate) alloy used in PF simulations are $c_\infty = 5.0$ wt%Nb, $k = 0.37$, $m = 9.0$ K/wt%Nb, $\Gamma = 2.49 \times 10^{-7}$ Km, $D = 2.44 \times 10^{-9}$ m²/s, $\epsilon_4 = 0.02$, with $T_M = 1670.43$ K and $T_0 = 1548.81$ K.

We solve Eqs. (3)-(4) under homogeneous Neumann (no-flux) boundary conditions along all directions. Moreover, the solid-liquid interface is initialized along the liquidus isotherm, with ψ initialized as the signed distance function to the liquidus isotherm (negative in the liquid region). The dimensionless supersaturation field is initialized based on the equilibrium concentration, i.e. $U(z, y, 0) = -1.0$. The computational domain Ω_m is a rectangle of dimensions $2.01w_s \times 1.01d_s$, e.g. $\Omega_m = 257 \mu\text{m} \times 97 \mu\text{m}$ in the case of the reference melt pool configuration, with the center of the melt pool at the center of the top boundary (as represented in Fig. 1). The total simulated time is equal to 2.5 milliseconds in all cases.

2.3.2. Polycrystalline grain growth: To consider the columnar grain growth competition in the melt pool, the two-dimensional (2D) orientation of grains is stored in an auxiliary integer field. It assumes a value of 0 in the liquid phase and an integer in the range of $[1, 90]$ in the solid phase, which is also used as a discrete set of misorientation angles of the grains, in degrees. When $(1 - \phi^2)$ exceeds a threshold, here 0.01, the grain index is updated according to the local neighborhood. This method creates a halo of orientation field in the liquid around a grain. When a grid point is allocated a solid grain index value higher than 0, the index field no longer evolves, and neither does the solid-solid grain boundary (GB). While it does not account for solid-state microstructure evolution, this method is a computationally efficient alternative to multi phase-field models [16], since it relies on a single phase field. Its use is appropriate in the presence of well-developed dendritic structures, with GBs forming deep within the mushy zone, i.e. when the macroscopic orientation of resulting GBs depends primarily on the growth competition of primary and secondary dendrite tips in the vicinity of the solidification front.

To initialize the grain index field, N_g number of points (Voronoi cell centers) are randomly distributed in Ω_m . A random integer value in the range of $[1, 90]$ is attributed to each point as the corresponding grain orientation. After the spatial discretization of Ω_m , the initial grain distribution is generated by a classic Voronoi tessellation algorithm. Finally, the grain orientation of computational cells located within the liquid region ($\psi < 0$) are reset to 0. The solution of Eqs (3)-(4) hence results in the epitaxial growth of columnar grains from the melt pool fusion line. Since we aim to assess the effect of initial grain size on the solidification microstructure, we considered different grain densities with $N_g = 750, 1500, 3000$ and 6000 , corresponding to equivalent grain radii between 1.15 and 3.25 μm . Moreover, in order to gain a better statistical picture of final grain structure, each simulation is repeated five times with different initial grain distributions, hence resulting in 60 PF simulations in total.

2.3.3. Implementation: Phase-field Eqs (3)-(4) are solved in two dimensions by the finite difference method on a uniform spatiotemporal grid using the Euler explicit time integration scheme. The time step size, Δt , is considered as 0.3 of the maximum time step size based on the stability of Laplacian operators. A standard second-order five-point stencil is used to discretize Laplacian operators. The rest of terms in Eqs (3) and (4) are discretized by central difference schemes (see appendices of Ref. [6] for details).

The diffuse interface width $W = 0.8 \Delta x$ and grid spacing Δx were determined based on a convergence study of the steady-state tip undercooling as a function of grid size in a unidirectional solidification with temperature gradient equal to its average in the mushy region and a pulling velocity equal to the scanning speed. Under conditions relevant to additive manufacturing, such a convergence study is quite limiting, since both the dendrite tip radius and the diffusion length are small. However, it is essential for the purpose of quantitative prediction of dendrite/cells growth kinetics and resulting grain structures. While the convergence study pointed at $\Delta x \approx 5$ nm for well-converged simulation in longitudinal simulations [8], here we can afford to use $\Delta x = 10$ nm, since isotherms and interface velocities are lower along the cross-section than they are along the longitudinal direction. Hence, the total number of spatial computational cells is equal to $25700 \times 9700 \approx 2.49 \times 10^8$ grid points in the case of the reference melt pool dimensions. While (y, z) dimensions are different, the total number of grid points is the same for the deep and wide configurations. The resulting time step is equal to 3×10^{-9} seconds, such that $O(10^5)$ time steps are required to complete the simulation.

Because of this grid size limitation for quantitative predictions, PF simulations at the scale of a full melt pool, even in 2D, are extremely computationally demanding. Therefore, advanced acceleration schemes are required. We implemented the model for massively parallel computing on multi-graphic processing units (Multi-GPU) with the computer unified device architecture (CUDA) programming language. Each simulation is performed on one computing node equipped

with four Nvidia RTX-3090 GPUs. We use a layer-wise domain decomposition to distribute computation load among GPUs, with the computational domain divided into 4 almost equal layers along the y -direction (and the same number of grid points along x). An extra halo grid layer is added to the top and bottom rows of each domain to simplify the imposition of boundary conditions and inter-GPU data communication. Halo layer data is updated using direct GPU-GPU communication, so as to avoid expensive GPU-to-CPU and CPU-to-GPU data transfers.

3. Results and Discussion

Figure 2 illustrates the evolution of the grain structure during competitive growth in a simulation for the reference melt pool size and a grain number $N_g = 750$. Figure 3 shows the final grain structures for one of the five simulation for each of the three considered melt pool sizes (reference, deep, and wide) and two considered initial grain numbers ($N_g = 750$ or 6000).

In all cases, the solid-liquid interface initially advances with a locally nearly-planar morphology at early stage. After a short time period, required for the development of a concentration boundary layer ahead of the interface, it destabilizes into cellular patterns. Several cells are eliminated early, leading to a rapid increase of the local primary spacing, while dendritic sidebranches appear after a short time. The average primary dendritic arm spacing (PDAS) was not found to markedly depend upon the initial grain density. Moreover, the iso-concentration line at $c = c_\infty$ in Fig. 2 (black line), which closely envelops the solidification front, shows that the diffusion length is of the same order or even smaller than the selected local primary spacings. While the diffusive conditions are an oversimplification of the transport regime in the melt pool — strong Marangoni convection is usually expected — this may provide an explanation for the typical lack of secondary sidebranches in additively manufactured metallic alloys.

A strong growth competition occurs between columnar grain in the melt pool. In qualitative agreement with the theory by Walton and Chalmers [1], grains with a $\langle 10 \rangle$ crystalline axis well aligned with the main heat transfer directions (i.e. perpendicular to the fusion line and isotherms) tend to prevail in the growth competition by eliminating the less favored grains with higher misorientation with the temperature gradient. In the case of the reference melt pool, the melt pool aspect ratio is close to unity (i.e. the fusion line is near circular). The resulting growth competition does not lead to a strong texture, as seen by the broad distribution of orientations present in the solidified melt pool (Fig. 3 a,b). In contrast, in the case of deep (Fig. 3 c,d) and wide (Fig. 3 e,f) melt pools, the growth competition results in a more noticeable $\langle 10 \rangle$ texture (apparent from the predominance of darker shades of red and blue). This $\langle 10 \rangle$ texture is primarily attributed to the large fraction of the melt pool solidifying under a mostly horizontal (Fig. 3 c,d) or vertical (Fig. 3 e,f) temperature gradient. The grain elimination mechanism proceeds via either dendrite impingement in the case of converging dendrites (grains) or side-branching in the case of diverging dendrites [6].

To further analyze texture selection, we quantified the orientation distributions in the different simulations. In Figure 4, histograms show normalized grain orientation (i.e. fraction of the melted area) with $N_{\text{bin}} = 10$ bins of width 9° , combining all grain densities (20 simulations per histogram). To illustrate the dependence upon initial grain densities, additional curves show idealized functions $H(\theta) = A \cos(4\theta) + 1/N_{\text{bin}}$, fitted to similar orientation distributions histograms within the five runs for each different initial grain density. The sole fitting parameter A may be interpreted as a measure of the strength of the $\langle 10 \rangle$ texture, with $A = 0$ corresponding to a flat distribution (no texture). This analysis confirm that deep ($A \approx 0.0749$) and wide ($A \approx 0.0855$) melt pools have a strong $\langle 10 \rangle$ texture (high population of grains with near 0 and 90 degrees orientations) in comparison to the reference melt pool geometry ($A \approx 0.0349$). Fitted curves for different N_g show that the effect of initial grain size on the final texture is marginal, with most values of A (all values for deep and wide cases) deviating by 20% or less from those obtained for the distributions combining all values of N_g (listed in parenthesis earlier).

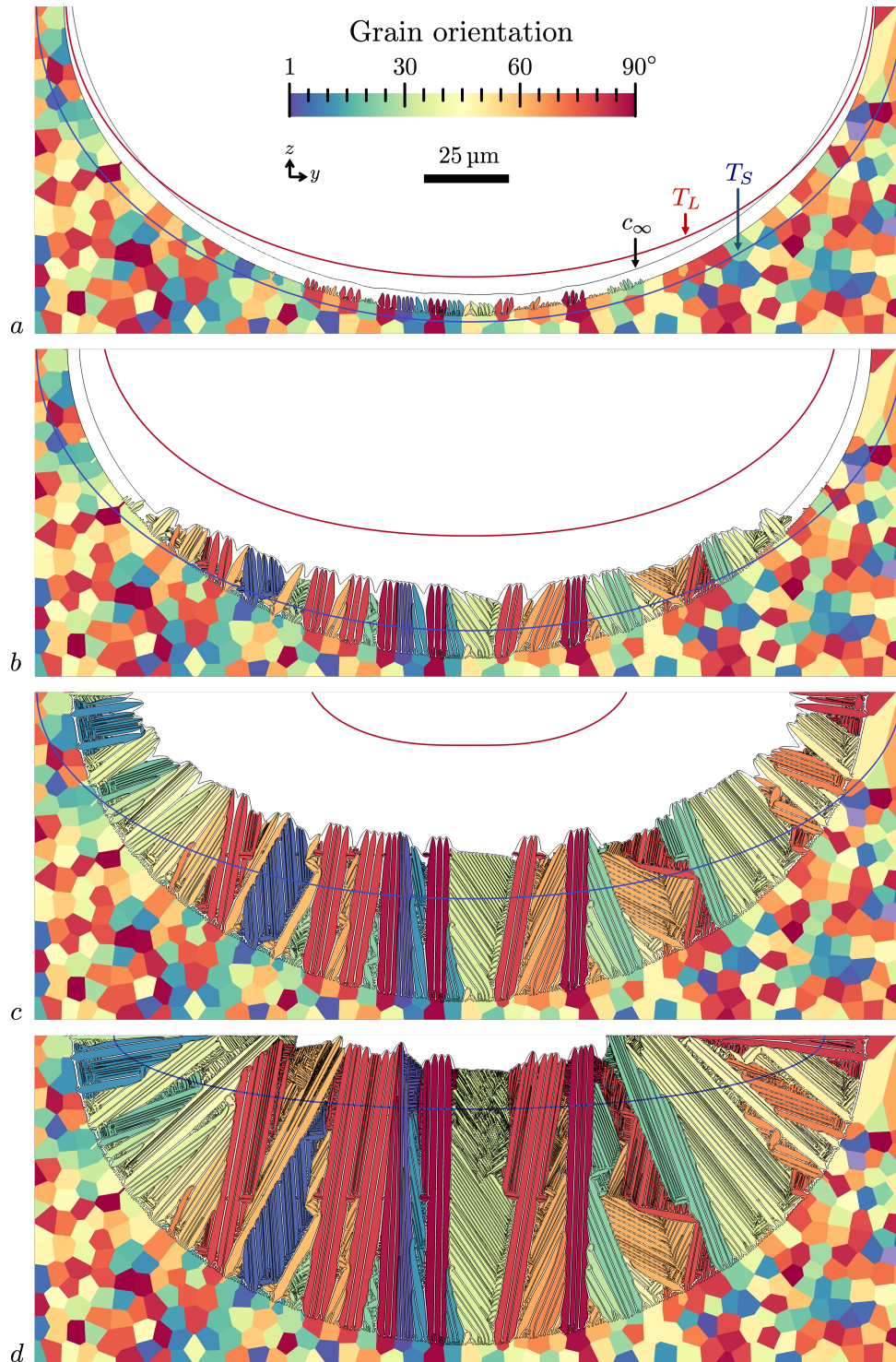


Figure 2. Evolution of grain structure with time for the reference melt pool size and $N_g = 750$, at $t =$ (a) 0.75, (b) 1.25, (c) 1.75, and (d) 2.25 ms. Solidus and liquidus isotherms are marked in blue and red line, respectively, and the iso-concentration $c = c_\infty$ appears as black line.

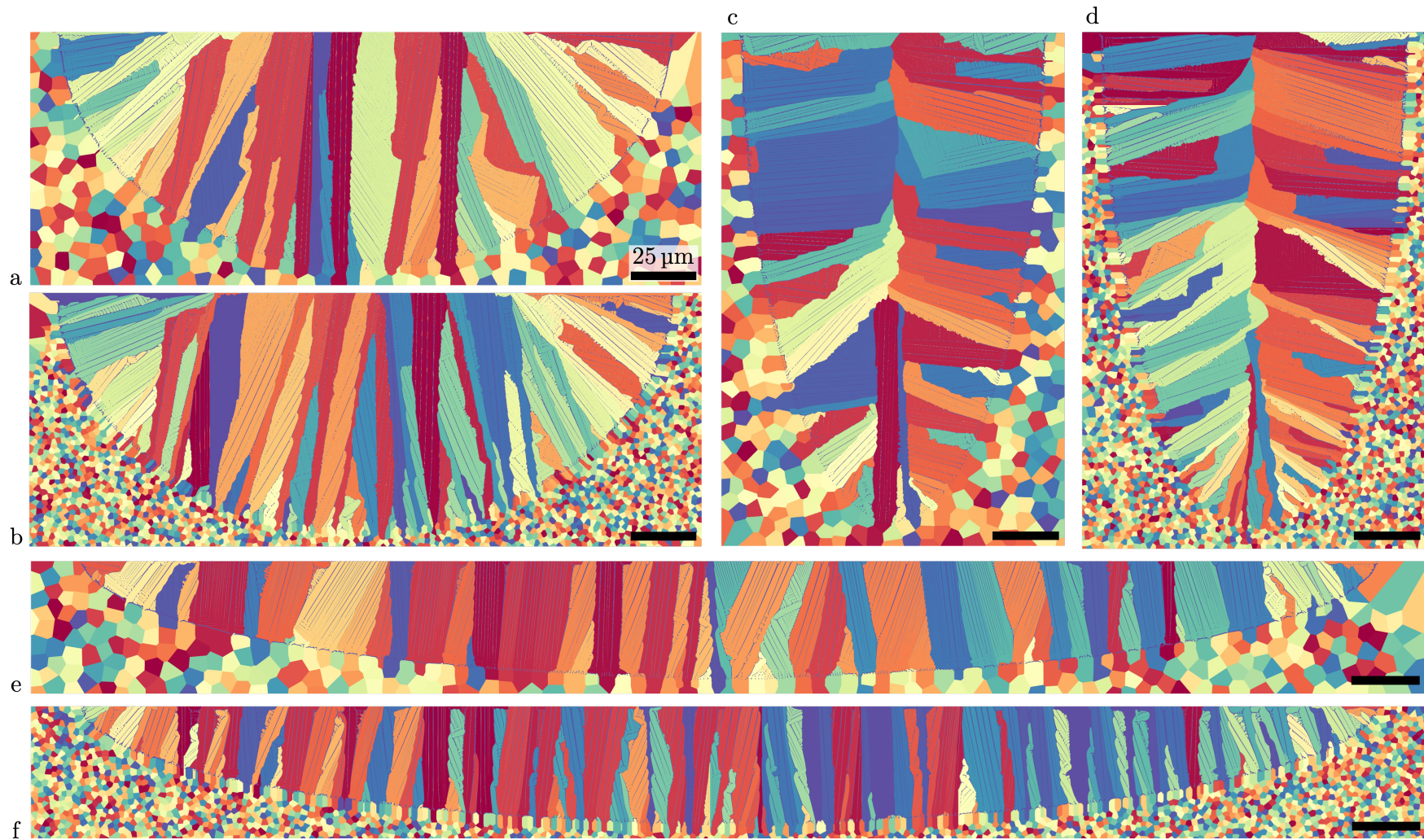


Figure 3. Representative final grain structures corresponding to reference (a,b), deep (c,d) and wide (e,f) melt pools with $N_g = 750$ (a, c, e) and $N_g = 6000$ (b, d, f). The grain orientation color map is similar to Fig. 2.

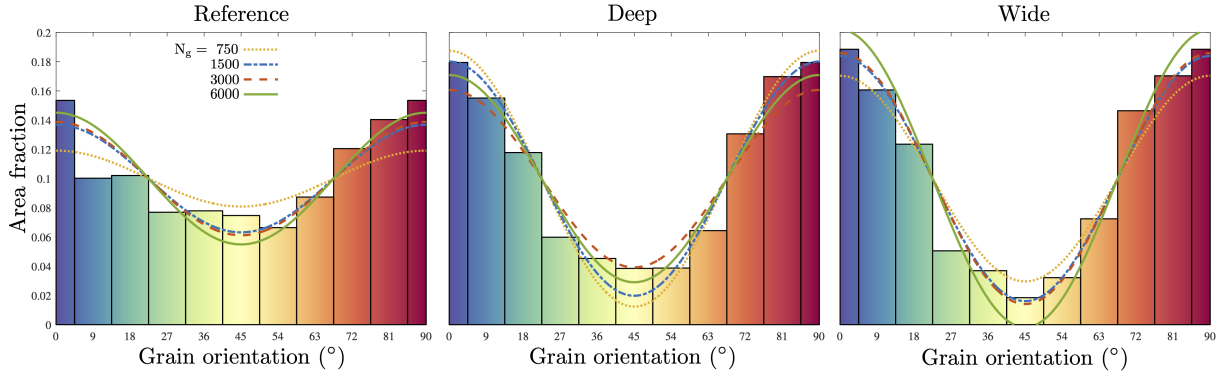


Figure 4. Histograms of grain orientations for reference (left), deep (center), and wide (right) melt pools. Each histogram shows the orientation distribution combining all four initial grain densities (20 simulations per histogram). Overlapped curves are the fitted cosine functions for the 4 different initial grain densities (5 simulations each). The grain orientation distributions are counted over each solid pixel and scaled by the total number of counted grid points, such that the ordinate axis corresponds to a fraction of the melt pool area. Considering the fourfold symmetry of the crystal structure, histograms are periodic with respect to the orientation angle, such that the leftmost and rightmost bins are similar and include angles from -4° (i.e. 86°) to 4° (i.e. 94°).

In the case of a deep melt pool, we can essentially divide the melt pool into two regions: a relatively texture-less bottom part with a circular/elliptical fusion line, and a textured upper part with a near vertical fusion line. As a result, the final $\langle 10 \rangle$ texture in the deep case is less strong compared to the wide melt pool, in which the main thermal gradient direction is essentially vertical. Interestingly, while these results show a clear texture transition from weak to strong $\langle 10 \rangle$ texture when the melt pool aspect ratio deviates from unity, they do not exhibit any indication of a transition toward other textures — such as, for instance, a possible $\langle 110 \rangle$ texture suggested from geometrical arguments and experimental hints [17, 18].

Finally, on the computational side, a preliminary scaling analysis shows a near linear scaling of the algorithm speedup with the number of GPUs. For instance, for the reference melt pool and $N_g = 6000$, the computational time is about 82, 43 and 22 hours using 1, 2 and 4 GPUs, respectively. Still, while the multi-GPU parallelization goes a long way in enabling full melt pool scale simulation in 2D, a similar 3D investigation remains unreasonable. Indeed, a single equivalent three-dimensional quantitative PF simulation at full melt pool scale would require a number of spatial grid points of $O(10^{13})$ and a similar number of time steps. Such a large-scale simulation, even using state-of-the-art petascale computing resources, would require $O(\text{day})$ to perform. It would therefore result in an enormous investment in time and resources for a relatively minor return in terms of physical insight into grain texture selection. For 3D simulations at this scale, coarse-grained approaches, e.g. cellular automaton, remain most convenient, while statistically capturing grain texture selection with reasonable accuracy [9].

4. Summary and Perspectives

We performed quantitative phase-field simulation of solidification in thermal conditions relevant to SLM processing of a Nickel alloy. We limited our micro-scale simulations to two-dimensional cross-sections of the melt pool (perpendicular to the scanning direction), using a thermal history at quasi steady-state computed by 3D finite element analysis, using CalPhaD-computed alloy parameters [8, 9]. We studied the effect of the melt pool geometry (i.e. its aspect ratio) and of the initial grain density along the fusion line on the final microstructure. According to our

results, a near-circular fusion line (i.e. an aspect ratio close to unity) does not lead to any notable texture, while relatively wider and/or deeper melt pools, which have more horizontally or vertically oriented fusion lines, promote the formation of a clear $\langle 10 \rangle$ texture.

Here, we only considered the single-track melting of a random Voronoi grain distribution. Therefore, the resulting grain texture is not completely representative of a realistic AM microstructure. Indeed, we decided to put the focus on the fundamental mechanisms of grain growth competition within a non-one-dimensional temperature field, which have received little attention so far. In order to produce a more realistic simulation of grain texture emergence from AM, one should account for multiple layers, multiple tracks, and nucleation events, all of which would be relatively straightforward to implement, as well as three-dimensional simulations, which, on the other hand, could be much more challenging computationally.

Perspectives following from this work are multiple. A three-dimensional quantitative phase-field study with the same level of accuracy (down to the level of individual dendrite) remains computationally prohibitive, and is thus unlikely to provide statistically-meaningful insight. However, even in two dimensions, the inclusion of additional physics into the simulations could certainly bring a fresh look onto grain growth competition within multidimensional temperature fields. For instance, including crystal nucleation in the melt pool would make it possible to study potential columnar-to-equiaxed transitions. The present study was also limited to the lower end of the velocity range relevant to SLM processing. In this low-velocity regime, the solid-liquid interface remains close to equilibrium, which is not always the case for typical SLM conditions. Ongoing work specifically focus on extending this kind of study to include kinetic undercooling and solute trapping using recent PF formulations [19, 20].

Acknowledgments

This work was supported by the Spanish Ministry of Science and the European Union NextGenerationEU (PRTR) through the MiMMoSA project (PCI2021-122023-2B) and a Ramón y Cajal fellowship (RYC2019-028233-I).

References

- [1] Walton D and Chalmers B 1959 *Trans. Am. Inst. Min. Metal. Eng.* **215** 447–457
- [2] D’Souza N, Ardakani M, Wagner A, Shollock B and McLean M 2002 *J. Mater. Sci.* **37** 481–487
- [3] Wagner A, Shollock B and McLean M 2004 *Mater. Sci. Eng. A* **374** 270–279
- [4] Zhou Y, Volek A and Green N 2008 *Acta Mater.* **56** 2631–2637
- [5] Li J, Wang Z, Wang Y and Wang J 2012 *Acta Mater.* **60** 1478–1493
- [6] Tourret D and Karma A 2015 *Acta Mater.* **82** 64–83
- [7] Takaki T, Ohno M, Shibuta Y, Sakane S, Shimokawabe T and Aoki T 2016 *J. Cryst. Growth* **442** 14–24
- [8] Elahi S, Tavakoli R, Boukellal A, Isensee T, Romero I and Tourret D 2022 *Comput. Mater. Sci.* **209** 111383
- [9] Elahi S, Tavakoli R, Romero I and Tourret D 2023 *Comput. Mater. Sci.* **216** 111882
- [10] Raghavan S, Singh G, Sondhi S and Srikanth S 2012 *Calphad* **38** 85–91
- [11] Ghosh S, Ma L, Ofori-Opoku N and Guyer J 2017 *Modell. Simul. Mater. Sci. Eng.* **25** 065002
- [12] Hong C 2019 *Computer modelling of heat and fluid flow in materials processing* (UK: CRC press)
- [13] Mills K 2002 *Recommended values of thermophysical properties for selected commercial alloys* (England: Woodhead Publishing)
- [14] Echebarria B, Folch R, Karma A and Plapp M 2004 *Phy. Rev. E* **70** 061604
- [15] Glasner K 2001 *J. Comput. Phys.* **174** 695–711
- [16] Steinbach I, Pezzolla F, Nestler B, Seeßelberg M, Prieler R, Schmitz G and Rezende J 1996 *Physica D* **94** 135–147
- [17] Jadhav S D, Dadbakhsh S, Goossens L, Kruth J, Van Humbeeck J and Vanmeensel K 2019 *J. Mater. Process. Technol.* **270** 47–58
- [18] Higashi M and Ozaki T 2020 *Mater. Des.* **191** 108588
- [19] Pinomaa T and Provatas N 2019 *Acta Mater.* **168** 167–177
- [20] Ji K, Dorari E, Clarke A and Karma A 2023 *Phys. Rev. Lett.* **130** 026203